





Identification and time-resolved study of ferrimagnetic spin-wave modes in a microwave cavity in the strong-coupling regime

Angelo Leo ^{1,2,*}, Anna Grazia Monteduro,^{1,2,3} Silvia Rizzato ^{1,2}, Luigi Martina ^{1,3} and Giuseppe Maruccio ^{1,2,3,*}

¹*Department of Mathematics and Physics, University of Salento, Via per Arnesano, 73100, Lecce, Italy*

²*CNR NANOTEC—Istituto di Nanotecnologia, Via per Arnesano, 73100 Lecce, Italy*

³*INFN—Sezione di Lecce, Via per Arnesano, 73100 Lecce, Italy*



(Received 11 July 2019; revised manuscript received 28 December 2019; published 27 January 2020)

Recently the hybridization of microwave-frequency cavity modes with collective spin excitations has attracted large interest for the implementation of quantum computation protocols, which exploit the transfer of information among these two physical systems. Here we investigate the interaction among the magnetization precession modes of a small yttrium iron garnet sphere and the microwave electromagnetic modes, resonating in a tridimensional aluminum cavity. In the strong coupling regime, anticrossing features were observed corresponding to various magnetostatic modes, which were excited in a magnetically saturated sample. Time-resolved studies show evidence of Rabi oscillations, demonstrating coherent exchange of energy among photonic and magnon modes. To facilitate the analysis of the standing spin-wave patterns, we propose here a procedure, based on the introduction of a scaling variable. The resulting easier identification of magnetostatic modes can be exploited to investigate, control, and compare many-level hybrid systems in cavity- and opto-magnonics research.

DOI: [10.1103/PhysRevB.101.014439](https://doi.org/10.1103/PhysRevB.101.014439)

I. INTRODUCTION

Combining different fundamental excitations is a recent route for quantum computation applications, with the promise to stimulate the development of new hybrid quantum technologies and protocols. Indeed, it was suggested that encoding information in different physical systems can provide advantages in overcoming the strict requirements in terms of decoherence timescales and capacity to process the information, which can be difficult to match together. In this respect, a crucial requirement is the achievement of a strong coupling regime between the respective fundamental excitations in two physical systems. Recent findings demonstrated the capability to obtain a robust hybridization among light quanta and different excitations at low temperature, by employing trapped atoms [1], nitrogen vacancy centers in diamonds [2], superconducting qubits [3], spin impurities in Si [4], and organic radicals [5,6]. In this framework, magnons exhibited strong stability in coupling with photons, when they are excited in ferro-/ferrimagnetic (FM) materials, especially if yttrium iron garnet (YIG) single crystals are used [7]. In contrast with paramagnetic spin ensembles, which at room temperature (RT) are weakly coupled to the photons, YIG presents at least a three orders greater net spin density, which permits to get the strong coupling. To couple spin waves (SWs) with electromagnetic (EM) signals, a convenient way is to confine the YIG in a three-dimensional (3D) microwave (MW) cavity [8]. It was reported that this yields the stable formation of two-level systems and magnon-cavity polaritons, as a consequence of the hybridization among MW photons and the fundamental

magnetostatic mode [also known as Kittel mode and corresponding to ferromagnetic resonance (FMR)] [9–15]. Even nonuniform magnetostatic modes (MSMs) can be sustained by the material depending on its shape, and they can be also coupled to cavity modes [16,17]. The resulting pattern of spectral features is more complex, and its association with specific modes can be not straightforward.

In the present work, we investigate the interaction among the magnetization precession modes in a small magnetically saturated YIG sphere and the MW electromagnetic modes resonating in a tridimensional aluminum cavity at room temperature. A rich spectrum characterized by several anticrossing features is observed because of the strong coupling regime in correspondence of various magnetostatic modes. Time-resolved studies show evidence of Rabi oscillations, demonstrating coherent exchanges of energy among photons and the involved magnon modes at RT. For facilitating the analysis of the stationary SW patterns, here we propose a procedure, based on the introduction of a scaling variable, related to the magnetic characteristics of the FM material and to the applied external electromagnetic field. Notably, plotting the data with respect to this variable, we obtain a direct identification of the involved MSMs.

II. EXPERIMENTAL SETUP AND CAVITY MODES

The investigated system is composed of a single crystal YIG sphere, 1 mm of diameter [18], located into an aluminum cavity with inner dimensions $44 \times 22 \times 9$ mm³. YIG (Y₃Fe₅O₁₂) is chosen for its peculiar characteristics. In particular, its magnetic moment comes from Fe⁺³ ions in the 6S_{5/2} ground state, and YIG behaves as a ferrimagnetic insulator with a 550 K Curie temperature, a typical saturation magnetization $M_S = 0.178$ T, spin density of 4.22×10^{27} m⁻³, and

*Corresponding authors: angelo.leo@unisalento.it, giuseppe.maruccio@unisalento.it

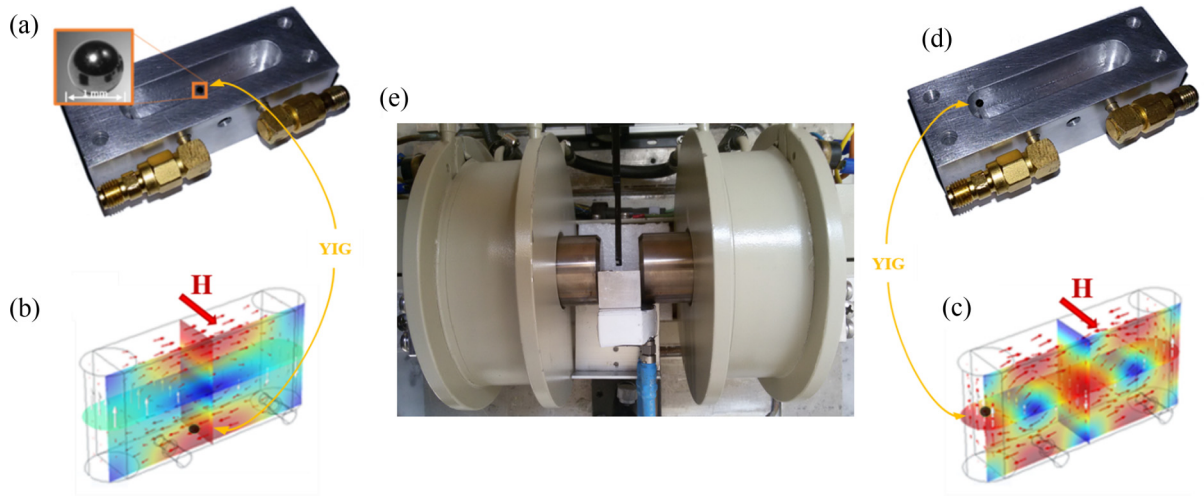


FIG. 1. (a) 3D aluminium semicavity loaded by a YIG sphere and (b) FEM-simulated MW magnetic field distribution for the loaded cavity at TE_{101} in a perpendicular static magnetic field H . (c) Semicavity loaded by YIG sphere on lateral side and (d) corresponding MW magnetic field for TE_{102} (black dots on FEM simulations refer to position of sphere, corresponding to the magnetic antinodes in the two configurations). (e) Experimental setup showing the loaded cavity between the electromagnet poles for application of the static magnetic field.

exchange constant $\alpha = 3 \times 10^{-12} \text{ cm}^2$ [19]. A crucial characteristic for the applications is the low magnetic damping and a correlated narrow linewidth of $2.3 \times 10^{-6} \text{ T}$ [19]. This property has favored the use of the YIG crystals in optical and radiofrequency devices, such as microwave oscillators, circulators, and optical isolators for many decades.

First, the YIG sphere is placed in a central position at the bottom of one semicavity of the ground wall as shown in Fig. 1(a). Such a position corresponds to the magnetic antinode for the fundamental (TE_{101}) mode [10], in order to maximize the interaction of magnonic modes with the MW field [Fig. 1(b)]. Then the cavity resonator is placed between the poles of a GMW electromagnet [Fig. 1(e)] generating a magnetostatic field, whose intensity is swept from 250 to 330 mT (with steps of 0.2 mT). Similarly, for further studies of the second (TE_{102}) mode, the YIG sphere is placed on one of the three TE_{102} magnetic antinodes, located on the junction plane of the two semicavities [this configuration is shown in Fig. 1(c)]. More precisely, the sphere is put close to the rounded wall of the resonator, on one of the lateral antinodes as shown in Fig 1(d). In this case, the magnetostatic field intensity is swept from 360 to 440 mT, in order to get the strong coupling regime. The resonator is excited with an Agilent MXG N5183A signal generator, while transmission measurements are performed with an Agilent MXA N9010 spectrum analyzer. Both devices are controlled with homemade LABVIEW software. Specifically, the frequency is swept in a range of 320 MHz, centered around the first (or the second) cavity eigenfrequency, at fixed magnetic field, and spectroscopic measurements were performed applying 0 dBm input power.

At room temperature, zero DC magnetic field, and loaded with the YIG sphere, experimentally the cavity exhibits the TE_{101} mode at $\omega_c/2\pi = 8.401 \text{ GHz}$ and the TE_{102} mode at $\omega_c/2\pi = 10.361 \text{ GHz}$. The loaded quality factor Q_L of the mere cavity with YIG at TE_{101} is 4000, with insertion loss $IL = -33.1 \text{ dB}$. This leads to an estimated intrinsic Q

factor $Q_i = Q_L/(1 - 10^{IL/20}) \simeq 4100$. The second mode exhibits a Q_L of 4300, with $IL = -30.16 \text{ dB}$ and $Q_i = 4450$. In these conditions, the system remains lossy coupled to the measurement setup. At both the TE_{101} and TE_{102} magnetic antinodes, the insertion of the YIG sphere does not perturb significantly the EM signal, in the absence of a drive magnetostatic field. Indeed, a resonant frequency shift of less than 0.1% is observed. Furthermore, the ratio between the crystal volume V_{YIG} and the magnetic modal volume V_c is $V_{\text{YIG}}/V_c \approx 2 \times 10^{-4}$, which also justifies the observed negligible variation of the quality factor.

III. STRONG COUPLING REGIME

The loaded-cavity spectrum as a function of the perpendicular magnetic field is reported in Fig. 2. While measuring at frequencies around the first photonic mode, sweeping of the magnetostatic field intensity gives a rich magnonic spectrum, which is characterized by the presence of anticrossings points around TE_{101} , as shown in the 2D map in Fig. 2(b). The FMR (known as the Kittel mode [9]) lies at 294.1 mT, as indicated by a yellow arrow, and exhibits a bright mode indicating a higher order interaction. Additionally, a series of MSMs are exhibited, which are shown with dotted yellow lines, whose separation gradually reduces towards lower magnetostatic fields. Figure 2(a) illustrates how the signal amplitude at TE_{101} varies as a function of the magnetic field: the transmitted electromagnetic signal takes the form of Fano resonances [20,21], and it is significantly reduced corresponding to the avoided crossings, with a splitting of the resonance peak [see Fig. 2(b)]. On the other hand, the 2D map at TE_{102} shows only a few clearly visible avoided crossings [Fig 2(c)], in addition to the main uniform precession resonance (FMR) at 391.0 mT, indicated with the yellow arrow. The relative signal amplitude from the cavity at TE_{102} as a function of static magnetic field is reported in Fig. 2(d).

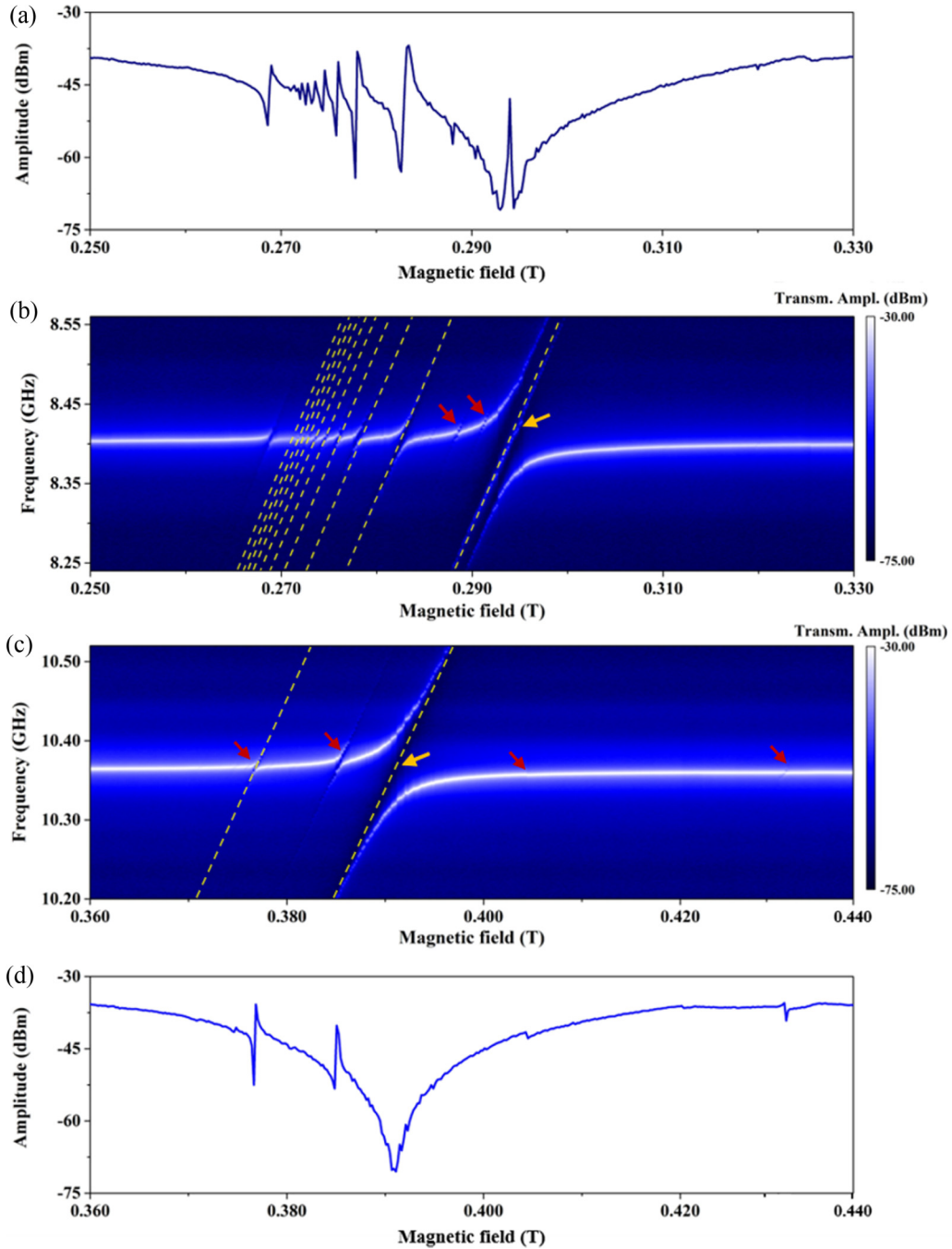


FIG. 2. (a) Transmission amplitude at $\text{TE}_{101} = 8.401$ GHz for magnetic field ranging from 250 to 330 mT. (b) Cavity response as a function of bias magnetic field and frequency near the fundamental TE_{101} mode. Dashed yellow lines and red arrows in the 2D maps of amplitude refers to identified MSMs in (m, m) and $(m + 1, m)$ families, respectively. (c) Cavity response near TE_{102} for magnetostatic field ranging from 360 to 440 mT. Here the $(3, 1)$ mode at higher static field is highlighted by a red arrow. (d) Transmission amplitude at $\text{TE}_{102} = 10.361$ GHz for magnetic field ranging from 360 to 440 mT (in the second configuration with sphere on cavity lateral side).

The avoided level crossings in the map of transmitted signal amplitude T can be described by means of an input-output formalism [11,15,22,23]:

$$T(\omega) = \frac{\kappa_c}{j(\omega - \omega_c) - \frac{1}{2}(2\kappa_c + \kappa_{\text{int}}) + \sum_i \frac{|g_i|^2}{-\frac{1}{2}\gamma_i + j(\omega - \omega_i)}}, \quad (1)$$

where $\kappa / 2\pi = (2\kappa_c + \kappa_{\text{int}}) = \omega_c / 2\pi Q_L$ is the photonic damping for each mode resonating at $\omega_c / 2\pi$, which takes into account the damping κ_c through the single connectors and the internal damping κ_{int} associated to the mere aluminium cavity, j is the imaginary unit number, the index i identifies a specific magnetostatic mode, whose frequency line width is γ_i , and the interaction strength of the hybrid mode for the

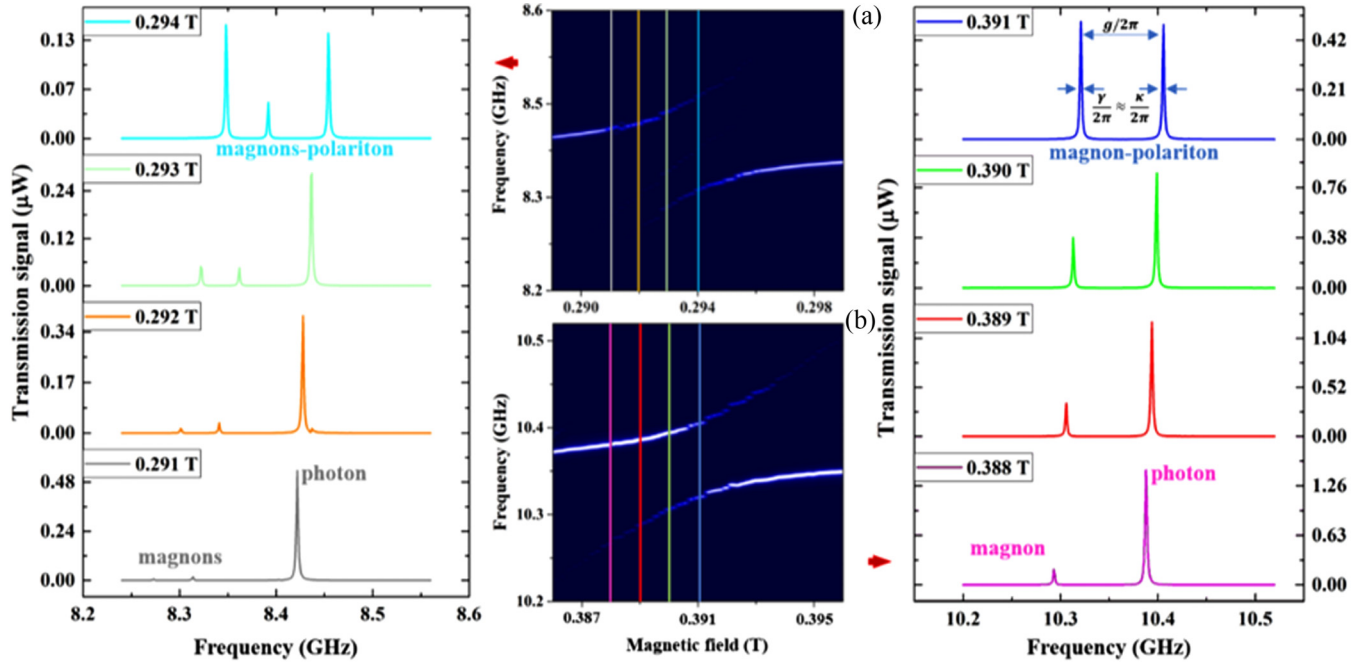


FIG. 3. Strong coupling between the fundamental magnetostatic mode in the YIG sphere and the TE₁₀₁ and TE₁₀₂ cavity modes. (a) 2D maps around TE₁₀₁ when the magnetostatic field ranges between 289 and 299 mT. The spectra corresponding to colored lines are shown on the left, where formation of magnon-polariton systems is shown. (b) 2D maps around TE₁₀₂ when the magnetostatic field ranges between 386 and 396 mT. The spectra corresponding to colored lines are shown on the right. When the systems are fully coupled, $g/2\pi$ is the frequency mismatch between the resonance peaks, and broadenings $\gamma/2\pi$ and $\kappa/2\pi$ of both standing waves modes are similar.

whole magnonic system is

$$\frac{g_i}{2\pi} = \frac{g_{0,i}\sqrt{N}}{2\pi} = \frac{[\eta\Gamma\sqrt{\frac{(\mu_0\hbar\omega_c)}{V_c}}]}{2\pi}\sqrt{N}, \quad (2)$$

which is related to the coupling strength $g_{0,i}/2\pi$ for a single interacting spin through the number N of net spins in the examined sample [24]. Notably, $\frac{g_i}{2\pi}$ refers to coupling strength between the two (magnonic and photonic) states and is evaluated as the frequency mismatch among the resonant peaks of the hybrid modes (Fig. 3, on the right). The quantity $\Gamma = g\mu_B/\hbar$ is the gyromagnetic ratio of spin ensemble, where g is the Landé g factor, μ_B is Bohr magneton, \hbar is the reduced Planck constant, and μ_0 is the vacuum permeability. The spatial overlap coefficient $\eta = \int_{\text{sphere}} \frac{\vec{H} \cdot \vec{M}}{H_{\text{max}}M_{\text{max}}V_{\text{YIG}}} dV$ between the two subsystems (i.e., cavity and sphere modes) is calculated taking into account the driving MW magnetic field \vec{H} and the complex time-dependent off- z axis sphere magnetization \vec{M} for the considered mode, while H_{max} and M_{max} correspond to their maximum values in the sphere volume V_{YIG} . As a further figure, the cooperativity of the two levels system is defined as $C_i = g_i^2/\gamma_i\kappa$.

In Fig. 3 details of the spectra of cavity toward hybridization, near the fundamental magnetostatic mode (FMR), are reported for cavity modes TE₁₀₁ and TE₁₀₂ at fields indicated with vertical lines of corresponding color. When the subsystems are fully coupled, $g/2\pi$ corresponds to the frequency mismatch between the resonance peaks, and broadenings $\gamma/2\pi$ and $\kappa/2\pi$ of both wave modes are comparable. In these conditions, obtained when the magnetostatic field intensity is 294.1 mT for the TE₁₀₁ and 391.0 mT for the TE₁₀₂ mode,

cavity dissipation rates $\kappa/2\pi$ are 3.2 and 3.0 MHz, respectively. Finally, the magnonic damping $\gamma/2\pi$ is 2.5 MHz. For a FM sphere, the uniform precession frequency $\omega_{\text{FMR}}/2\pi$ is related to the external field H_0 by $\frac{\omega_{\text{FMR}}}{2\pi} = \Gamma H_0$ [25]. Since the cavity mode frequencies and $\omega_{\text{FMR}}/2\pi$ must match when the two subsystems are strongly coupled, it is then possible to estimate the gyromagnetic ratio Γ by posing $\omega_{\text{FMR}} = \omega_c = 2\pi\Gamma H_0$, and by substituting the corresponding H_0 values, then we obtain $\Gamma \approx 28.76$ GHz/T for the YIG sphere with respect to the value 28 GHz/T reported in Ref. [26]. In Table I the magnetostatic fields as well as the evaluated coupling parameters, photonic/magnonic dampings, and cooperativity C are summarized for all the observed anticrossing points (this will be discussed in more detail in the next section with reference to the MSM identification).

IV. IDENTIFICATION OF MSM

In order to identify and analyze the magnetization precession phenomena corresponding to the observed anticrossing features, a discussion in terms of magnetostatic theory is useful [26–29]. The MSMs' resonant frequencies f (and dispersion relation of SW modes, generally) in spheroids inserted in MW cavity working at frequency $\omega_c/2\pi$ can be derived from the characteristic equation in terms of associated Legendre functions $P_n^m(f, H_0)$:

$$n + 1 + \xi_0 \frac{P_n^m(f, H_0)}{P_n^m(f, H_0)} \pm m \frac{\Gamma f M_S}{\Gamma^2 H_i^2 - f^2} = 0, \quad (3)$$

TABLE I. Summary of obtained parameters for TE₁₀₁ mode.

| H_0 (T) | MSM-TE ₁₀₁ | $\gamma/2\pi$ (MHz) | $\kappa/2\pi$ (MHz) | $g/2\pi$ (MHz) | C | Period of oscillations (ns) | Frequency of oscillations (MHz) |
|-----------|-----------------------|---------------------|---------------------|----------------|--------|-----------------------------|---------------------------------|
| 0.2718 | (9, 9) | 3.9 | 4.0 | 2.05 | 0.27 | 370 | 2.70 |
| 0.2722 | (8, 8) | 2.9 | 4.2 | 2.35 | 0.45 | 369 | 2.71 |
| 0.2728 | (7, 7) | 3.1 | 3.3 | 2.90 | 0.82 | 275 | 3.64 |
| 0.2734 | (6, 6) | 3.1 | 3.1 | 3.55 | 1.31 | 258 | 3.88 |
| 0.2746 | (5, 5) | 3 | 3.1 | 4.35 | 2.03 | 222 | 4.50 |
| 0.2760 | (4, 4) | 3.1 | 2.8 | 5.45 | 3.42 | 176 | 5.70 |
| 0.2780 | (3, 3) | 2.5 | 2.5 | 7.20 | 8.29 | 127 | 7.89 |
| 0.2826 | (2, 2) | 1.6 | 2.3 | 12.55 | 42.80 | 80 | 12.51 |
| 0.2941 | (1, 1) _{FMR} | 2.5 | 3.2 | 25.35 | 80.33 | 39 | 25.64 |
| 0.2943 | (1, 1) _{FMR} | 2.5 | 3.2 | 29.45 | 108.42 | 35 | 28.47 |

where $H_i = H_0 - M_S/3$, $\xi_0 = (1 + \frac{H_i}{M_S} - \frac{f^2}{\Gamma^2 M_S H_i})^{1/2}$, and $P_n^{m'}(f, H_0) = \frac{dP_n^m(f, H_0)}{d\xi_0}$.

The index $n \in \mathbb{N}$ labels localization of MSM on the surface with respect to the external magnetostatic field \vec{H}_0 , while m ($|m| \leq n$) refers to the angular momentum, whose value could attributed to the presence of *magnetic quasivortices* on the sphere [30]. The MSMs relative to indexes n and m are then labeled as (n, m) and are grouped in *families* as a function of the value $n - |m|$. In general, the relation between the resonant frequencies of MSM and the external magnetic field is not linear, except for the mode families $n - |m| = 0$ and 1. In these cases, Eq. (3) assumes the following simplified forms:

$$\frac{f}{\Gamma M_S} - \frac{H_{0,mm}}{M_S} + \frac{1}{3} = \frac{m}{2m+1} \quad (n = m), \quad (4)$$

$$\frac{f}{\Gamma M_S} - \frac{H_{0,m(m+1)}}{M_S} + \frac{1}{3} = \frac{m}{2m+3} \quad (n = m+1). \quad (5)$$

Equation (4) with fixed $n = m = 1$ gives $f = \frac{\omega_{\text{FMR}}}{2\pi} = \Gamma H_{0,11}$, corresponding to uniform magnetization precession.

If the FM sphere is immersed in a confined magnetic field oscillating at frequency $\omega_c/2\pi$ and a strong coupling regime is reached at $H_{0,mm}$, the resonance frequencies of the two subsystems must match. By imposing this condition it is possible to determine the indexes m and n of the MSMs associated to each anticrossing. Thus, after extrapolating the $H_{0,mm}$ values associated to the various anticrossings observed at $f \approx \omega_{101}/2\pi = 8.405$ GHz for the map at TE₁₀₁ reported in Fig. 2(a) [31], a preliminary identification of (m, m) MSM can be carried out. Accordingly to Eq. (4), by using approximate values for Γ (also estimated from $H_{0,11} = \frac{\omega_{\text{FMR}}}{2\pi\Gamma}$) and M_S (0.178 T in literature) [26], we exploit the discrete nature of the indexes to facilitate association. Moreover, analyzing the (m, m) MSM, the spacing of nine consecutive splittings as a function of the external field is observed to decrease, moving far from FMR condition in Fig. 2. Subsequently, the trend of the magnetostatic field $H_{0,mm}$ corresponding to (m, m) MSM anticrossing conditions [Fig. 4(a)] is exploited to evaluate the saturation magnetization M_S , as a fitting parameter for Eq. 4 [32].

However, the identification of the involved MSM following this procedure is not immediate and hinders further analysis from Fig. 2. Starting from this observation and the previously discussed theory, for a more straightforward identification of

the different MSM, here we propose as an ansatz to rearrange data in order to plot the resonator signal as a function of cavity frequency and $[H_{0,mm} - (\frac{\omega_c}{2\pi\Gamma} - M_S/6)]^{-1}$ [Fig. 4(b)]. The reason is that [according to mathematical manipulations of Eqs. (4) and (5)], this is expected to bring be equally spaced features for each family when $n - |m| = 0$ or 1, as is demonstrated from the results shown in Fig. 4(b). In this frame, the identification of MSM of (m, m) and $(m+1, m)$ families at $\omega_{101}/2\pi$ is more direct. As a further improvement, in Fig. 4(c) the signal is plotted as a function of $-1/2 + M_S/4[H_{0,mm} - (\frac{\omega_c}{2\pi\Gamma} - M_S/6)]^{-1}$, which is obtained by a rearrangement of Eq. (4). It results that the local minima in oscillations of cavity amplitude are shown on an x axis now indicative of the mode (m, m) index, clearly visible until the ninth excitation. Notably, in this procedure, even if for M_S a value from literature is employed, the discrete nature of the indexes would allow a simple association of the mode.

For $(m+1, m)$ MSM identification, the magnetic field axis should be modified following Eq. (5). In this case, the main differences with the previous calculation are the presence of $-3/2$ as coefficient and a scaling of $3/4$ instead of $-1/2$ and $1/4$, respectively. Apparently, several features corresponding to modes $(4+3k, 3+3k)$, $k \in \mathbb{N}$, are detected up to m equal to 27. However, the most pronounced absorptions are limited to a few recognizable modes, which are degenerate with respect to other (m, m) ones; thus these features could be also ascribed to the latter. Only smaller $(m+1, m)$ MSM signatures can be distinguished separately in Fig. 2(a) (see red arrows), as the (5, 4) and (6, 5) modes. As a result, we conclude that the $(m+1, m)$ MSM family is less coupled to the cavity.

In Table I the identified (m, m) MSMs observed for the YIG sphere within the cavity for the first transverse electric mode are reported together with their corresponding magnetostatic fields, coupling parameters, and photonic/magnonic dampings. Since for coupling with the Kittel mode a bright mode is exhibited, the corresponding coupling strength is reported as two frequency mismatches among the two external branches and the central bright mode itself. Typically, a strong coupling regime is associated to coupling strength g values greater than the magnonic and the photonic damping γ and κ . In our case, this condition is fulfilled up to the (6, 6) MSM. It is also possible to discuss this aspect in terms of the cooperativity of the two-level system, which is defined as $C_i = g_i^2/\gamma_i\kappa$ with value 1 as threshold for a strong coupling

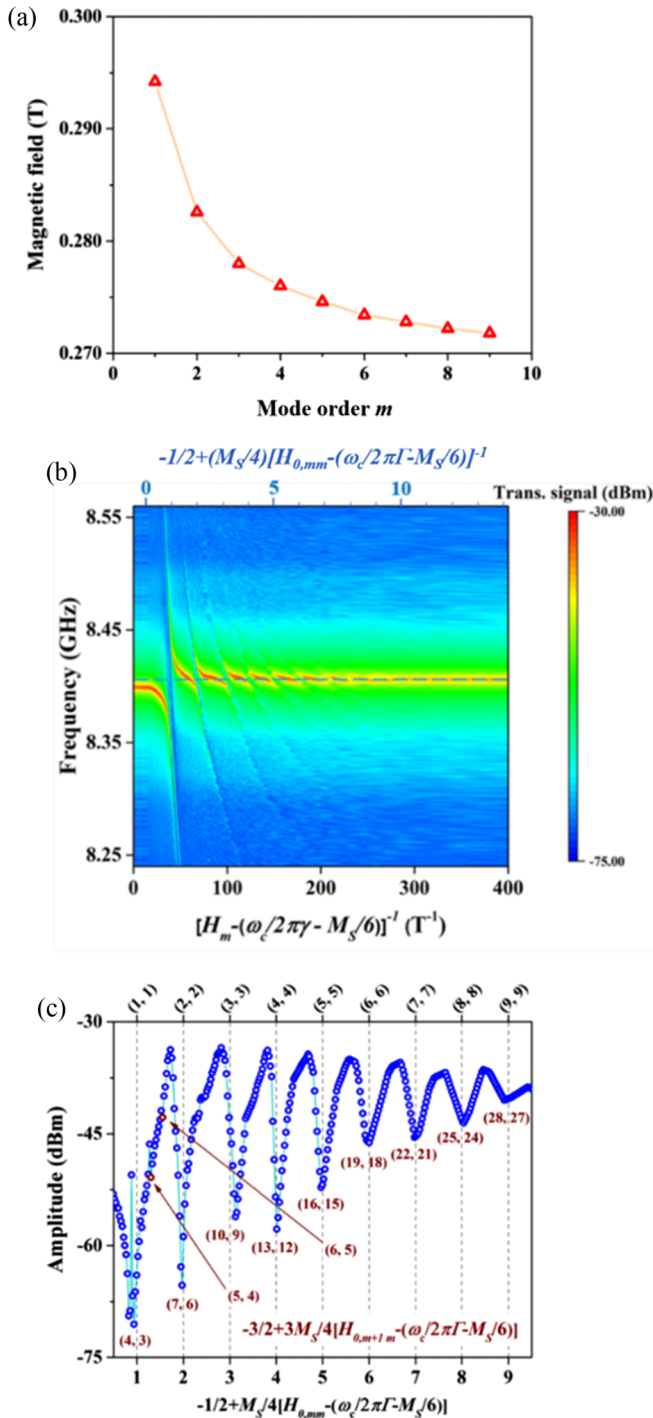


FIG. 4. (a) Trend of the magnetic fields at resonance conditions as a function of (m, m) MSM order at TE_{101} . (b) 2D map as a function of frequency near TE_{101} and the introduced scaling variable. In this frame, MSMs appear equally spaced. (c) At 8.405 GHz, (m, m) modes are recognized up to $m = 9$. On the other hand, $(m + 1, m)$ excitations are not all visible (only the one corresponding to indexes shown in red and in large part being degenerate with (m, m) modes).

regime. Notably we obtained cooperativity values even larger than 100 for the coupling among $(1, 1)_{\text{FMR}}$ and TE_{101} modes; then cooperativity decreases but still remains higher than 1 up to the $(6, 6)$ MSM. Cooperativity C among FMR and TE_{101}

is at least one order greater than values at other frequency splittings. Moreover, the photonic and magnonic losses were estimated to be comparable for all the different MSM modes.

V. TIME-RESOLVED MEASUREMENTS

For further insight into the strong coupling regime, we investigate also the time evolution of the strongly coupled system. Specifically, for time-resolved measurements, after sweeping the magnetic field to a specific value, we excited the cavity at resonance with the same signal generator used for the spectroscopic measurements, but now in combination with an Agilent 81150A pulse function generator in order to apply a pulsed $3 \mu\text{s}$ signal modulated at the cavity resonance frequency and cyclically pulse the signal in the cavity. The input amplitude was set at 10 dBm. An ultrafast digital sampling oscilloscope (Tektronix DSA8300), equipped with a 80E04 dual-channel time domain reflectometry sampling module and triggered by the same pulse function generator, was then employed to record the time-resolved signal by sampling every 125 ps and using the “envelope” acquisition mode, in which the oscilloscope retains the running minimum and maximum values in adjacent sample intervals, creating an envelope of all waveforms acquired for the channel. For each value of the magnetostatic field, we set the oscilloscope to collect the signal over 250 acquisitions.

The spin ensemble dynamics heavily influences the signal amplitude and both rise and fall times of cavity signal, as also reported in Ref. [33]. In Fig. 5(a) the cavity response at TE_{101} is shown: for lower values of the magnetostatic field, the signal is weakly modified, then it significantly grows for all the pulse duration, with a sensitive increase of cavity relaxation timescale. Successively, by a further increasing of the field, the signal drastically reduces and then increases again, and this phenomenon is repeated many times corresponding to the anticrossing fields. The proposed ansatz also was employed to facilitate analysis of this set of (time-resolved) measurements leading to Fig. 5(b), where MSMs up to $(9, 9)$ are visible as increased absorptions [34]. As example, the time scan relative to the coupling among the MW cavity TE_{101} and the $(2, 2)$ magnetostatic mode is shown in Fig. 5(c). Periodic fluctuations of the cavity signal amplitude during charging and relaxation of the system are clearly visible. These oscillations are a further indication of on-resonance hybridization among magnons and photons, which is reached when $\omega_c/2\pi = f_{\text{magnon}}$, resulting in a Rabi splitting in two peaks at energies $\hbar/2\pi(\omega_c \pm g_i)$. The energy stored inside the cavity decays in an exponential manner, but with periodic oscillations among the two states, demonstrating coherent exchange of energy among photon and magnon modes. In Fig. 5(d) the transients related to the relaxation of the cavity coupled with each (m, m) mode at given intensities of the static field are reported. Interaction with the Kittel mode of the sphere is reported two times being related to a higher order interaction between FMR and cavity resonance. Beyond FMR, signal oscillations are visible also for coupling with other MSMs, at least up to $(6, 6)$ mode, but with a different characteristic frequency and periods that increase as the mode index increases. In Table I the periods of cavity signal oscillations are reported for each (m, m) MSM along with the relative frequency of oscillation,

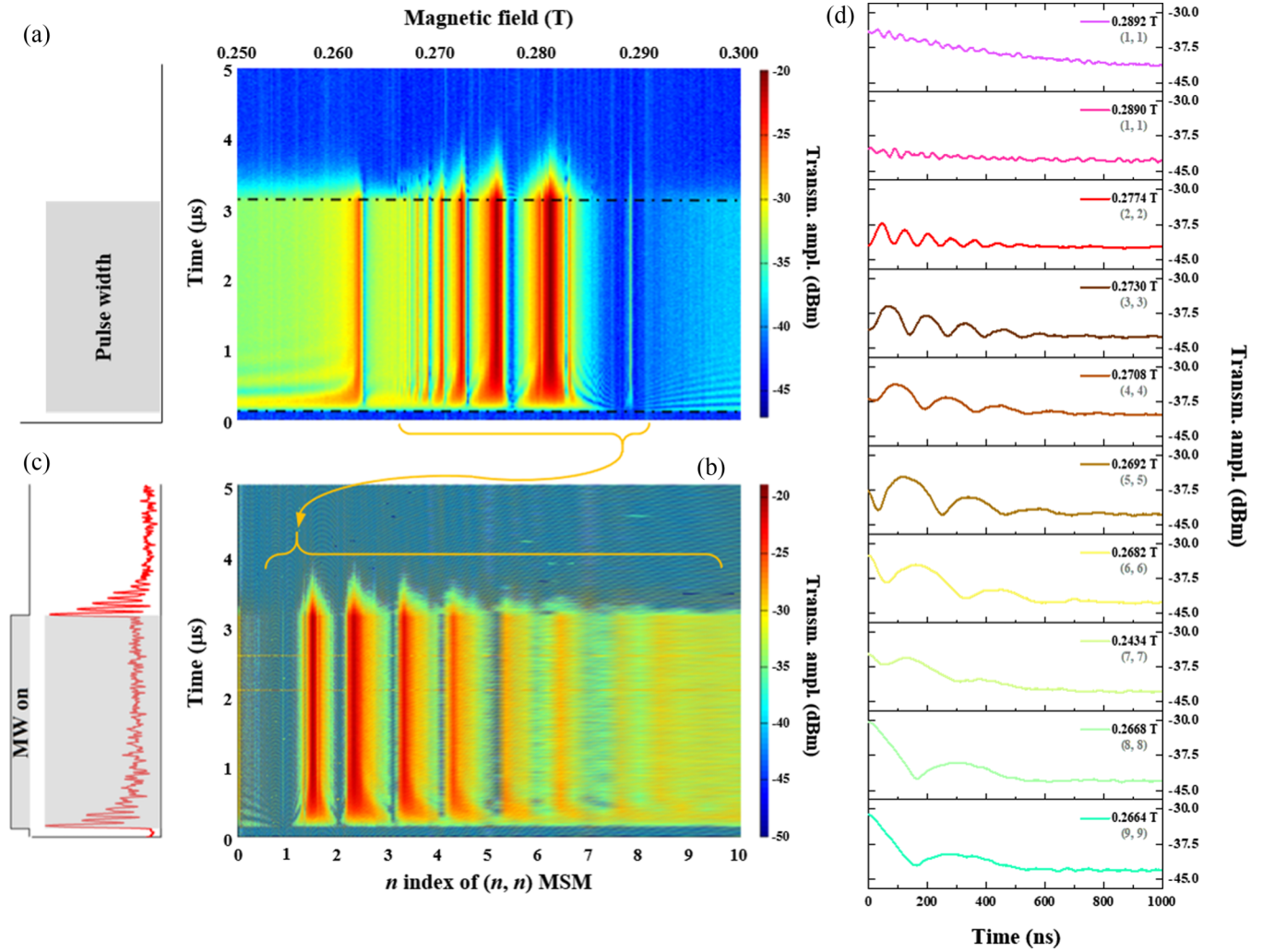


FIG. 5. (a) Transmission of a rectangular $3 \mu\text{s}$ microwave pulse at TE_{101} through the cavity versus time and magnetic field. (b) Time-resolved 2D map with x axis rescaled as a function of MSM index (c) Dynamics at resonance corresponding to strong coupling between TE_{101} cavity mode and $(2, 2)$ MSM. (d) Damped oscillations of signal when cavity MWs are strongly coupled with (m, m) MSMs.

which can be compared to the coupling strength obtained from spectroscopic measurements. Notably, values are very close with relative frequency mismatch between spectroscopic evaluation and time-resolved investigation below 1.3%. In addition to the observation of oscillations for various modes, this agreement is a clear indication of the physical origin of these features attributed to Rabi oscillations. For coupling with Kittel mode, due to a higher order interaction resulting in a bright mode at 0.2891 T, the oscillations at 0.2890 and 0.2892 T exhibit a dephasing of $\pi/2$, while it is the sum of the two oscillation frequencies which correspond to half of the 109.6 MHz splitting among the branches observed in spectroscopic measurements.

VI. CONCLUSION

The strong interaction regime between MSM modes excited in an YIG sphere and photonic modes in a 3D cavity resonator was investigated at RT. A rich spectrum was observed with several anticrossing features due to coupling to the

fundamental FMR mode as well as additional magnetostatic modes. As an ansatz for enabling a simple identification of the various MSMs, we proposed a rescaling procedure in order to plot the resonator signal as a function of cavity frequency and a scaling variable, just from a mathematical rearrangement of the eigenvalue equations for the MSMs in a spheroid [for both the (m, m) and $(m + 1, m)$ families]. This procedure was applied to both the frequency-dependent and time-resolved scans in a magnetic field and allowed us to recognize the (m, m) modes as the ones more coupled to the cavity. Magnetostatic fields, coupling parameters, photonic/magnonic dampings, and cooperativity C were evaluated for all modes up to the $(9, 9)$ one. Rabi oscillations were clearly visible in time scans, demonstrating (at RT) coherent exchange of energy among photons and the involved magnon modes. The easier identification of magnetostatic modes can be exploited to investigate, control, and compare many-level hybrid systems in cavity- and optomagnonics research [35–38].

ACKNOWLEDGMENTS

This work was financially supported by the MIUR-PRIN Project (prot.2012EF5HK4) and Regione Puglia NABIDIT—

NANOBIOTECNOLOGIE e SVILUPPO PER TERAPIE INNOVATIVE project (F31D08000050007), L.M. was partially supported by the INFN-IS MMNLP.

-
- [1] Y. Dudin and A. Kuzmich, *Science* **336**, 887 (2012).
- [2] S. Putz, D. O. Krimer, R. Amsuess, A. Valookaran, T. Noebauer, J. Schmiedmayer, S. Rotter, and J. Majer, *Nat. Phys.* **10**, 720 (2014).
- [3] T. Niemczyk, F. Deppe, H. Huebl, E. P. Menzel, F. Hocke, M. J. Schwarz, J. J. Garcia-Ripoll, D. Zueco, T. Hümmer, and E. Solano *et al.*, *Nat. Phys.* **6**, 772 (2010).
- [4] A. Bienfait, J. J. Pla, Y. Kubo, M. Stern, X. Zhou, C. C. Lo, C. D. Weis, T. Schenkel, M. L. W. Thewalt, and D. Vion *et al.*, *Nat. Nanotechnol.* **11**, 253 (2016).
- [5] A. Ghirri, C. Bonizzoni, F. Troiani, N. Buccheri, L. Beverina, A. Cassinese, and M. Affronte, *Phys. Rev. A* **93**, 063855 (2016).
- [6] C. Bonizzoni, F. Troiani, A. Ghirri, and M. Affronte, *J. Appl. Phys.* **124**, 194501 (2018).
- [7] D. A. Bozhko, A. A. Serga, P. Clausen, V. I. Vasyuchka, F. Heussner, G. A. Melkov, A. Pomyalov, V. S. L'vov, and B. Hillebrands, *Nat. Phys.* **12**, 1057 (2016).
- [8] A. Leo, S. Rizzato, A. G. Monteduro, and G. Maruccio, in *Three-Dimensional Magnonics: Layered Micro-and Nanostructures*, edited by G. Gubbiotti (Jenny Stanford, New York, 2019), pp. 347–376.
- [9] C. Kittel, *Phys. Rev.* **73**, 155 (1948).
- [10] X. Zhang, C.-L. Zou, L. Jiang, and H. X. Tang, *Phys. Rev. Lett.* **113**, 156401 (2014).
- [11] Y. Tabuchi, S. Ishino, T. Ishikawa, R. Yamazaki, K. Usami, and Y. Nakamura, *Phys. Rev. Lett.* **113**, 083603 (2014).
- [12] Y.-P. Wang, G.-Q. Zhang, D. Zhang, T.-F. Li, C.-M. Hu, and J. Q. You, *Phys. Rev. Lett.* **120**, 057202 (2018).
- [13] X. Zhang, C.-L. Zou, N. Zhu, F. Marquardt, L. Jiang, and H. X. Tang, *Nat. Commun.* **6**, 8914 (2015).
- [14] M. Goryachev, W. G. Farr, D. L. Creedon, Y. Fan, M. Kostylev, and M. E. Tobar, *Phys. Rev. Appl.* **2**, 054002 (2014).
- [15] N. Lambert, J. Haigh, and A. Ferguson, *J. Appl. Phys.* **117**, 053910 (2015).
- [16] X. Zhang, C. Zou, L. Jiang, and H. X. Tang, *J. Appl. Phys.* **119**, 023905 (2016).
- [17] R. Morris, A. van Loo, S. Kosen, and A. Karenowska, *Sci. Rep.* **7**, 11511 (2017).
- [18] The single-crystal YIG sphere of 1 mm diameter is even used as standard reference material for calibration of magnetometers; the certificate of analysis is reported in <https://www-s.nist.gov/srmors/certificates/2853.pdf>.
- [19] V. Cherepanov, I. Kolokolov, and V. L'vov, *Phys. Rep.* **229**, 81 (1993).
- [20] U. Fano, *Phys. Rev.* **124**, 1866 (1961).
- [21] E. Kamenetskii, G. Vaisman, and R. Shavit, *J. Appl. Phys.* **114**, 173902 (2013).
- [22] M. Harder, L. Bai, C. Match, J. Sirker, and C. Hu, *Sci. China Phys. Mech. Astron.* **59**, 117511 (2016).
- [23] D. F. Walls and G. J. Milburn, *Quantum Optics* (Springer Science & Business Media, Berlin Heidelberg, 2007).
- [24] G. S. Agarwal, *Phys. Rev. Lett.* **53**, 1732 (1984).
- [25] D. D. Stancil and A. Prabhakar, *Spin Waves* (Springer, New York, 2009).
- [26] P. Rösschmann and H. Dötsch, *Phys. Status Solidi B* **82**, 11 (1977).
- [27] P. Fletcher and R. Bell, *J. Appl. Phys.* **30**, 687 (1959).
- [28] R. L. White, *J. Appl. Phys.* **31**, S86 (1960).
- [29] L. Walker, *Phys. Rev.* **105**, 390 (1957).
- [30] A. Osada, A. Gluppe, Y. Nakamura, and K. Usami, *New J. Phys.* **20**, 103018 (2018).
- [31] Slightly shifted from 8.401 GHz due to proximity to strong coupling condition.
- [32] The estimated value of gyromagnetic ratio is 28.76 GHz/T, while the experimental value of saturation magnetization is 0.176 T.
- [33] C. Match, M. Harder, L. Bai, P. Hyde, and C.-M. Hu, *Phys. Rev. B* **99**, 134445 (2019).
- [34] Values estimated from time-resolved set of data: gyromagnetic ratio 29.24 GHz/T, saturation magnetization 149.49 mT.
- [35] Z.-X. Liu, C. You, B. Wang, H. Xiong, and Y. Wu, *Opt. Lett.* **44**, 507 (2019).
- [36] Y. Yang, J. W. Rao, Y. S. Gui, B. M. Yao, W. Lu, and C.-M. Hu, *Phys. Rev. Appl.* **11**, 054023 (2019).
- [37] B. Bhoi, B. Kim, S.-H. Jang, J. Kim, J. Yang, Y.-J. Cho, and S.-K. Kim, *Phys. Rev. B* **99**, 134426 (2019).
- [38] Y. Cao and P. Yan, *Phys. Rev. B* **99**, 214415 (2019).